Leveraging Compatible Iridium(III) Complexes to Boost Performance of Green Solvent-Processed Non-Fullerene Organic Solar Cells

Hao Xia, Miao Zhang,* Huaxi Wang, Yingjie Sun, Zikang Li, Ruijie Ma, Heng Liu, Top Archie Dela Peña, Hrisheekesh Thachoth Chandran, Mingjie Li, Jiaying Wu, Xinhui Lu, Wai-Yeung Wong,* and Gang Li*

In organic solar cells (OSCs), the short exciton lifetime poses a significant limitation to exciton diffusion and dissociation. Extending exciton lifetime and suppressing recombination are crucial strategies for improving the OSC performance. Herein, an effective approach is proposed by introducing the phosphorescent emitter, tris(2-(4-(tert-butyl)phenyl)-5-fluoropyridine)Iridium(III), with long-lived triplet exciton lifetime in OSCs. This research reveals that the steric structure of *fac*-Ir(tBufppy)$_3$ exhibits excellent compatibility with both the donor PM6 and acceptor BTP-eC9, maintaining efficiencies of over 90% even with a 30% third component loading. Moreover, a 10% addition of *fac*-Ir(tBufppy)$_3$ mitigates excessive aggregation in the acceptor BTP-eC9, optimizing the active layer morphology and improving the fill factor. Transient absorption spectroscopy and transient photoluminescence measurements demonstrate that the introduction of *fac*-Ir(tBufppy)$_3$ significantly extends exciton lifetimes and suppresses recombination, which increases the short-circuit current (J_{SC}). Ultimately, employing the non-halogenated solvent o-xylene for processing, an impressive power conversion efficiency (PCE) of 18.54% is achieved in devices based on PM6:10%*fac*-Ir(tBufppy)$_3$:BTP-eC9, surpassing the efficiency of binary PM6:BTP-eC9 devices (17.41%). This work provides a promising approach to further improve the PCEs in binary OSCs by introducing a phosphorescent iridium(III) complex as the third component.

1. Introduction

Organic solar cells (OSCs) were considered a promising photovoltaic technology due to their key advantages of solution processing, lightweight, flexibility, and transparency.[1–4] Over the last decade, the power conversion efficiency (PCE) of OSCs has witnessed remarkable progress, owing to the development of new materials, innovations in device engineering, fabrication processes, and a deeper understanding of device physics.[5–8] Particularly noteworthy is the recent advancement with the development of fused-ring acceptors, enabling OSCs to achieve a performance ≈20%.[9] These advancements offer the potential for the near-future commercialization of OSCs. Nevertheless, OSCs continue to face challenges, including a short exciton lifetime and difficulties in modifying the morphology of the active layer.[10–14] These issues are crucial constraints that hinder the further development of OSCs.

H. Xia, R. Ma, H. T. Chandran, G. Li
Department of Electrical and Electronic Engineering
Research Institute of Smart Energy (RISE)
Photonic Research Institute (PRI)
The Hong Kong Polytechnic University
Hung Hum, Kowloon, Hong Kong 999077, China
E-mail: gang.w.li@polyu.edu.hk

M. Zhang, H. Wang, Y. Sun, Z. Li, W.-Y. Wong
Department of Applied Biology and Chemical Technology and Research
Institute for Smart Energy
The Hong Kong Polytechnic University
Hung Hum, Kowloon, Hong Kong 999077, China
E-mail: bjtumiao.zhang@polyu.edu.hk; wai-yeung.wong@polyu.edu.hk

H. Liu, X. Lu
Department of Physics
The Chinese University of Hong Kong
New Territories, Hong Kong 999077, China

T. A. Dela Peña, J. Wu
The Hong Kong University of Science and Technology
Function Hub
Advanced Materials Thrust
Nansha, Guangzhou 511400, P. R. China

**ADVANCED
SCIENCE NEWS**

www.advancedsciencenews.com

**ADVANCED
FUNCTIONAL
MATERIALS**

www.afm-journal.de

As widely recognized, exciton diffusion is a crucial process in OSCs for converting solar energy into electrical energy, hence playing a significant role in determining the photovoltaic efficiency of OSCs.[15] The exciton diffusion length (L_d) can be calculated using the formula $L_d = \sqrt{D\tau}$, where D represents the diffusion coefficient, and τ is proportional to the average photoluminescence (PL) lifetime within the thin film.[16] Hence, the exciton lifetime serves as a critical parameter in determining L_d. However, it is generally observed that the generation of excitons in the active layer of OSCs occurs in the singlet state. The lifetimes of single excitons in many semiconducting polymers typically fall within the range of 10–100 ps, resulting in the corresponding diffusion lengths of 5–10 nm.[17] This characteristic propensity makes excitons prone to recombination before reaching the donor/acceptor (D/A) interface, resulting in energy losses and adversely affecting the efficiency of OSCs. Therefore, a critical approach for elongating the lifetime and L_d of excitons as a strategic approach for enhancing the performance of organic solar cells is needed. One important strategy to augment the L_d involves the utilization of long-lived triplet excitons.[18] In many luminescent materials, particularly phosphorescent materials, long-lived triplet excitons can be generated upon excitation, with metal complexes being the most classic examples.[19–21] Therefore, in recent years, some research teams have introduced metal complexes capable of generating long-lived triplet excitons into OSCs to enhance their efficiency.[22,23] For instance, in a previous fullerene system, Huang et al. incorporated trace amounts of an iridium complex into PTB7, achieving a PCE of 8.71% for the PTB7Ir1:PC$_{71}$BM-based device.[21] Tao et al. presented the tris-Ir(III) complex TBz3Ir, characterized by an extended triplet lifetime and enhanced hole mobility. When blended with Y6, the binary OSCs exhibited a PCE of 11.35%.[22] In our previous work, we introduced iridium complexes into the polymer main chain of PM6, synthesizing PM6Ir1. The addition of an appropriate amount of M1 enhanced photon harvesting, triplet exciton lifetime, and charge mobility, and optimized the active layer morphology. As a result, the OSCs based on PM6Ir1:Y6 exhibited a remarkable PCE of 16.71%.[23]

Furthermore, morphology control presents another significant challenge in OSCs.[24–27] Due to the limited diffusion distance of exciton and the inherently low charge carrier mobility of organic semiconductors, achieving an appropriate active layer morphology emerges as a key factor for attaining high-efficiency OSCs. Recent reports in the literature suggest that ternary strategies represent one of the most effective approaches for regulating the active layer morphology.[28–30] Additionally, there are studies indicating substantial enhancements in OSC efficiency by introducing a small quantity of metal complexes

into the polymer backbone to optimize the active layer morphology. For instance, Peng et al. incorporated a small amount of Pt(Ph)$_2$(DMSO)$_2$ into the polymer and synthesized Pt-PSFTZ.[31] This modification increased steric hindrance along the polymer main chain, inhibited polymer aggregation, regulated phase separation, optimized morphology, and consequently improved device efficiency to 16.35%. Min et al. incorporated different concentrations of iridium (Ir) complexes into PM6, resulting in a set of π-conjugated polymer donors named PM6-Ir0.5, PM6-Ir1, PM6-Ir2.5, and PM6-Ir5.[32] The best device based on PM6-Ir1:Y6 (1:1.2, w/w) exhibited an outstanding PCE of 17.24%. However, in the aforementioned studies, it was observed that excessive incorporation of metal complexes (greater than 10%) had adverse effects, leading to reductions in FF and J_{SC}. This may be attributed to the poor compatibility between the metal complexes and PM6 and Y6.[33] Therefore, synthesizing phosphorescent materials that are highly compatible with the acceptors and can generate long-lived triplet excitons presents a significant challenge.

Hence, in this work, we synthesized a spatially stereo-structured complex, *fac*-Ir(tBufppy)$_3$, and observed its excellent compatibility with the donor PM6 and acceptor BTP-eC9 (**Figure 1**). Even with the addition of 30%, the efficiency remained over 90% of the optimal efficiency. The introduction of 10% *fac*-Ir(tBufppy)$_3$ optimized the active layer morphology leading to enhanced FF. Additionally, transient absorption spectroscopy and transient PL measurements indicated a significant extension in exciton lifetime with the introduction of *fac*-Ir(tBufppy)$_3$, effectively suppressing exciton recombination. Ultimately, by employing the non-halogenated solvent o-xylene (O-XY) for processing, devices based on PM6:10%*fac*-Ir(tBufppy)$_3$:BTP-eC9 achieved an impressive PCE of 18.54%, surpassing the efficiency of binary PM6:BTP-eC9 devices (17.41%). This study demonstrates a successful approach to synergistically prolonging exciton lifetime and modifying the morphology of the active layer to improve the device's performance.

2. Results and Discussion

2.1. Synthesis, Optical and Electrochemical Properties

The synthesis route for *fac*-Ir(tBufppy)$_3$ is outlined in Scheme S1 (Supporting information). Compounds 1 and 2 were procured from an organic reagent supplier. Compound 3 was obtained through Suzuki coupling between compounds 1 and 2. Compound 3 was subjected to a bridging reaction to yield compound 4, followed by a debridging reaction to obtain the final yellow product, *fac*-Ir(tBufppy)$_3$. All synthetic details are provided in the Electronic Supporting Information (ESI). Comprehensive characterization of all products was performed using ^{1}H-NMR, and additionally, ^{13}C-NMR and MALDI-TOF mass spectrum and single crystal structure were employed for product confirmation. *Fac*-Ir(tBufppy)$_3$ was soluble in common solvents such as chlorobenzene, O-XY, dichloromethane, and chloroform. *Fac*-Ir(tBufppy)$_3$ shows good thermal stability with a high decomposition temperature of 387 °C for its 5% weight loss, as illustrated by the thermogravimetric analysis curve in Figure S1 (Supporting Information). This behavior indicates that the prepared

T. A. Dela Peña, M. Li
Department of Applied Physics
The Hong Kong Polytechnic University
Kowloon, Hong Kong 999077, P. R. China
T. A. Dela Peña
Department of Chemistry
The Hong Kong University of Science and Technology
Kowloon, Hong Kong 999077, P. R. China
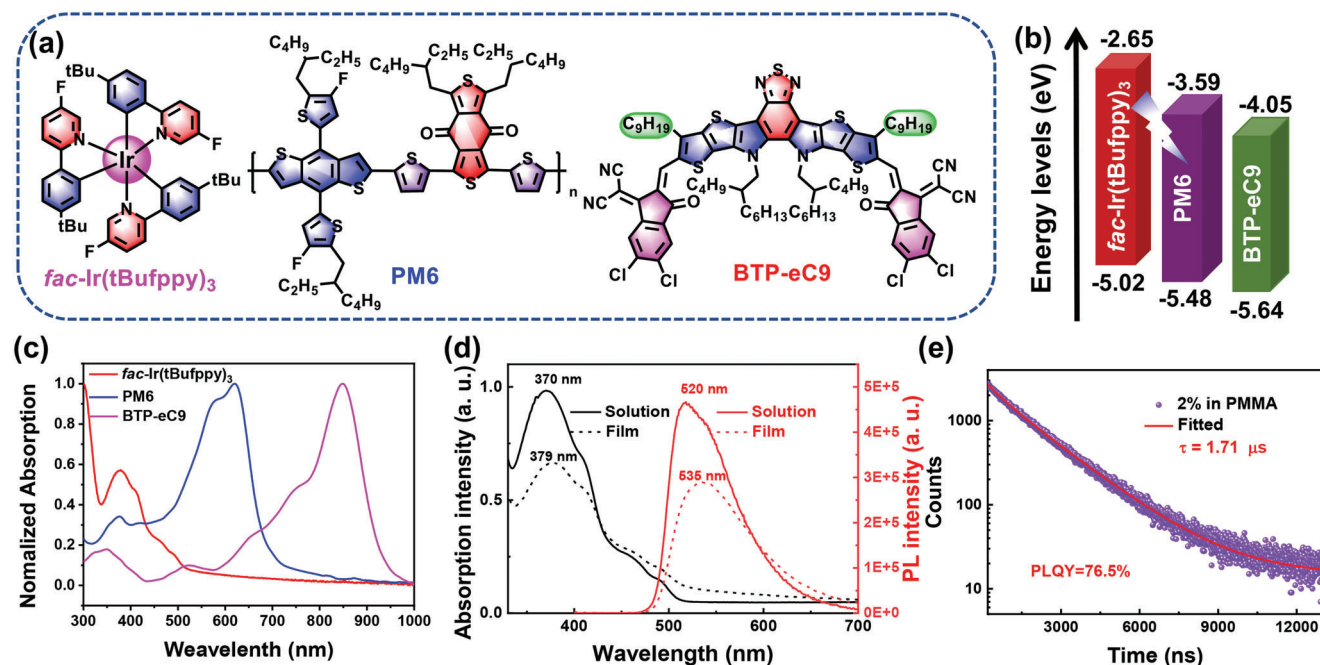
Figure 1. a) Molecular structure, b) energy levels of *fac*-Ir(tBufppy)$_3$, PM6 and BTP-eC9, c) absorption spectra of *fac*-Ir(*t*Bufppy)$_3$, PM6 and BTP-eC9 in films, d) absorption spectra and PL spectra of *fac*-Ir(tBufppy)$_3$ in toluene solution and neat film, e) transient decay of *fac*-Ir(tBufppy)$_3$ in PMMA film.

iridium(III) complex has good thermal stability for the fabrication of organic photovoltaics.

The optical characteristics of *fac*-Ir(tBufppy)$_3$, PM6, and BTP-eC9 were investigated through UV–vis–near-infrared (UV–vis–NIR) absorption spectra in thin films (Figure 1c), and the corresponding optical data are summarized in **Table 1**. *Fac*-Ir(tBufppy)$_3$ exhibits absorption in the range of 350–500 nm, complementing the absorption profiles of PM6 and BTP-eC9. The optical band gap (E_g^{opt}) of *fac*-Ir(tBufppy)$_3$ is calculated to be 2.37 eV. In the blend films, an increase in the concentration of *fac*-Ir(tBufppy)$_3$ corresponds to enhanced absorption, suggesting improved photon harvesting capabilities. In both solution and film, *fac*-Ir(tBufppy)$_3$ exhibited minimal shifts in the position of its absorption and PL peaks (Figure 1d), a characteristic likely attributed to its stable 3D structure. Moreover, the PL spectra of *fac*-Ir(tBufppy)$_3$ covered a range of ≈470–650 nm, entirely overlapping with the absorption spectrum of PM6. This alignment strongly suggests the possibility of energy transfer between *fac*-Ir(tBufppy)$_3$ and PM6.

The electrochemical potentials of *fac*-Ir(tBufppy)$_3$ were determined through cyclic voltammetry analysis (Figure S2, Supporting Information). The highest occupied molecular orbital (HOMO) level of *fac*-Ir(*t*Bufppy)$_3$ is calculated using the onset oxidation by employing an empirical equation, resulting in values of 5.02 eV. The lowest unoccupied molecular orbital (LUMO) level of *fac*-Ir(tBufppy)$_3$ is calculated to be 2.65 eV according to the absorption cutoff. The HOMO and LUMO levels of PM6 and BTP-eC9 were obtained from referenced reports,[34] as illustrated in Figure 1b. These energy levels demonstrate an ordered cascade, potentially facilitating efficient exciton dissociation and charge transfer.

2.2. Single Crystal Structure Analysis and Theoretical Calculations

The single crystal structure (Figure S3, Supporting Information) reveals that *fac*-Ir(tBufppy)$_3$ is a homoleptic tris-cyclometalated iridium(III) complex with a facial configuration. The details of crystal data, atomic coordinates, bond lengths, and angles are reported in the Cambridge crystallographic database (number: 2 264 431). The iridium(III) center is coordinated by three identical $\widehat{CN}$ ligands, forming a distorted octahedral coordination geometry. This spatial geometry effectively prevents molecular packing or aggregation, providing an explanation for the similar spectral range and shape observed in absorption and PL measurements of *fac*-Ir(tBufppy)$_3$ in both solution and film states.

Table 1. Photophysical properties of *fac*-Ir(*t*Bufppy)$_3$.

Complex	E_g [eV][a]	λ_{abs}^{max}[nm][b]	λ_{PL}^{max}[nm][c]	Φ_{PL} [%][d]	T [µs][e]	κ_r [10^5 s^{-1}][f]	κ_{nr} [10^5 s^{-1}][f]
fac-Ir(*t*Bufppy)$_3$	2.37	370/379	520/535	76.5	1.71	4.47	1.41

[a] Calculated by the equation: $E_g = 1240/\lambda$, λ is absorption threshold; [b] Peak wavelength in solution/film absorption; [c] Peak wavelength in solution/film PL; [d] PL quantum yield in PMMA (2 wt.% complex doping) using an integrating sphere; [e] Observed decay lifetime in PMMA film was fitted by the double fit exponential function: $\tau = 12.97\%\tau_1 +87.03\%\tau_2$ ($\tau_1 = 0.85$ µs, $\tau_2 = 1.85$ µs); [f] $k_r = \Phi_{PL}/\tau$, $k_{nr} = (1 - \Phi_{PL})/\tau$ (k_r and k_{nr} denote the radiative and non-radiative rate, respectively).
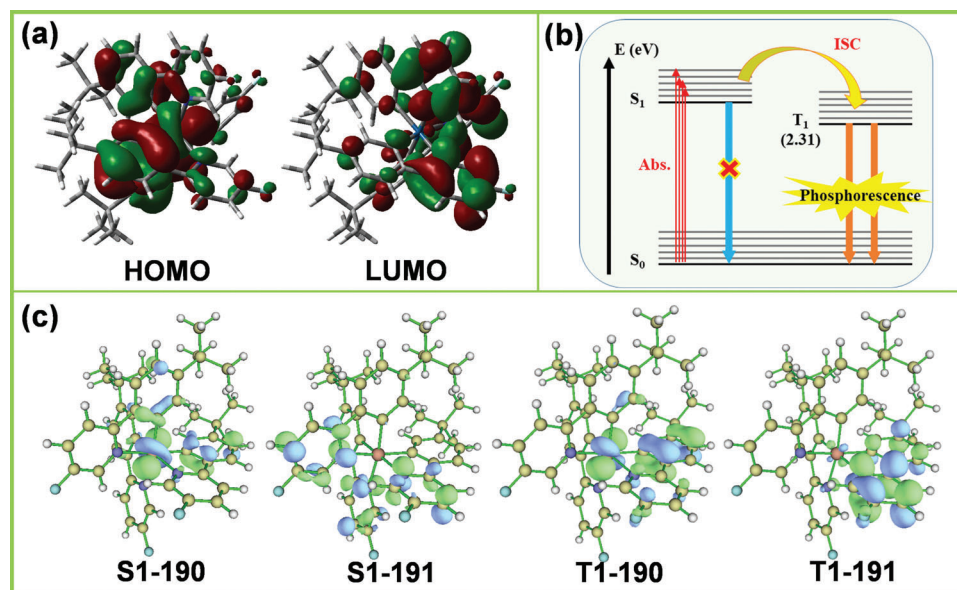
Figure 2. a) HOMO and LUMO energy levels of the electron cloud distribution of *fac*-Ir(tBufppy)$_3$. b) Schematic diagram of phosphorescence emission principle. c) Natural transition orbital (NTO) analysis of *fac*-Ir(tBufppy)$_3$.

In Figure S3 (Supporting Information, black), only several intermolecular short-range interactions are observed between *fac*-Ir(tBufppy)$_3$ molecules, involving a C–C distance of 3.3 Å, C–F distance of 3.0 Å, and C–H distance of 2.7 Å.
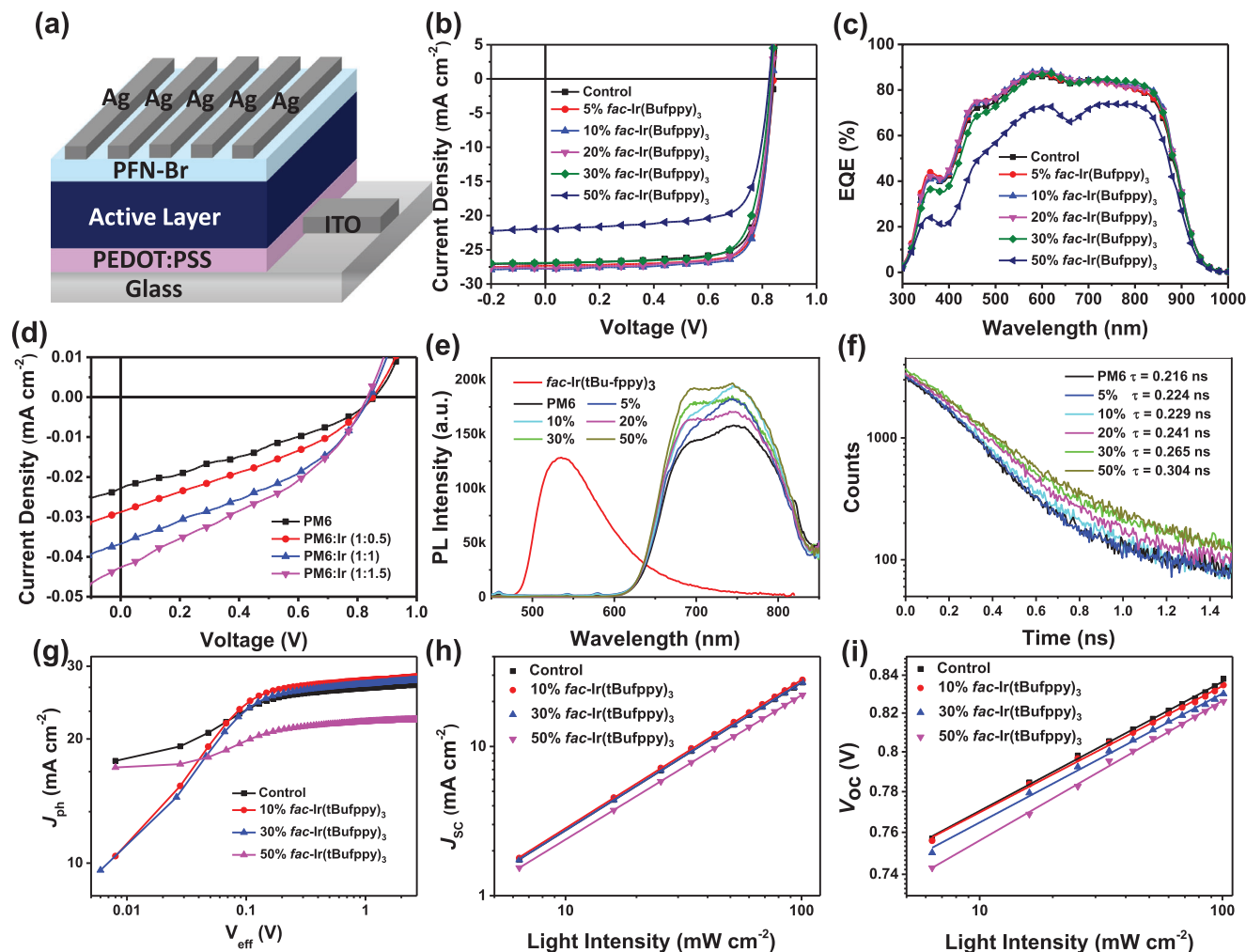
According to the single crystal structure of *fac*-Ir(tBufppy)$_3$, density functional theory (DFT) calculations were conducted by employing the Gaussian software package with the GENECP/PBELPBE basis set. The calculated distributions of HOMO and LUMO for *fac*-Ir(tBufppy)$_3$ are illustrated in **Figure 2a**. The HOMO is primarily located in the iridium center (Ir) and the tert-butyl-substituted benzene unit (Ph-tBu), while the LUMO predominantly resides in the fluorine-substituted pyridine unit (Py-F). Consequently, the absorption behavior of *fac*-Ir(tBufppy)$_3$ can be ascribed to the synergistic effects arising from both metal-to-ligand charge transfer (MLCT) and ligand-to-ligand charge transfer (LLCT) transitions.

For a comprehensive insight into the electronic structures and absorption characteristics of *fac*-Ir(tBufppy)$_3$, a natural transition orbital (NTO) analysis was conducted using time-dependent density functional theory based on the optimized S$_0$ geometry. The distributions of hole (H) and particle (P) orbitals for the lowest singlet and triplet states (S$_1$ and T$_1$) are depicted in Figure 2c, and the corresponding calculated data are summarized in Table S1 (Supporting Information). In the excited state S$_1$, the hole orbital is predominantly situated on the Ir center (≈44%) and the Ph-tBu unit (≈36%), while the particle orbital is primarily contributed by the Py-F unit (≈75%). Consequently, the high-energy absorption of *fac*-Ir(tBufppy)$_3$ is attributed to a combination of MLCT [dπ(Ir) → π*(Py-F)] and LLCT [π(Ph-tBu) → π*(Py-F)] transitions. The orbital distributions of the excited state T$_1$ exhibit a similar scenario to that of S$_1$. The hole orbitals of T$_1$ predominantly reside in the Ir center (≈27%) and the Ph-tBu unit (≈28%), while the particle orbital is mainly contributed by the Py-F unit (≈47%). As a result, the low-energy absorption of *fac*-Ir(tBufppy)$_3$ is ascribed to a mixture of triplet-metal-to-ligand charge transfer

(³MLCT) [dπ(Ir) → π*(Py-F)] and triplet-ligand-to-ligand charge transfer (³LLCT) [π(Ph-tBu) → π*(Py-F)] transitions.

The Ir(III) complexes have been widely demonstrated as effective phosphorescent compounds with longer triplet decay times compared with the singlet emission of many organic molecules. As described above, *fac*-Ir(tBufppy)$_3$ exhibits an intense absorption intensity in the UV region below 400 nm, so photogenerated excitons by itself have a low contribution in the process of photo-to-electric conversion due to both the low irradiance power and light transmittance of ITO substrate in this region. However, *fac*-Ir(tBufppy)$_3$ exhibits a strong PL ability covering from 500 to 650 nm, which overlaps with the absorption spectra of the host materials, especially the donor of PM6. This part of the energy can be well utilized through the effective Förster energy transfer processes between *fac*-Ir(tBufppy)$_3$ and PM6 (or BTP-eC9), contributing to the photocurrent increase of the corresponding OSCs.[35] The emission property of *fac*-Ir(tBufppy)$_3$ was carefully investigated using both the DFT calculation and experimental test through the Edinburgh FS5 Spectrofluorometer. The calculated emission energy is ≈2.3 eV from the lowest triplet characteristics of *fac*-Ir(tBufppy)$_3$, which is well matched with the emission peak at 535 nm of *fac*-Ir(tBufppy)$_3$ in the film state. The DFT results demonstrate that *fac*-Ir(tBufppy)$_3$ exhibits phosphorescent characteristics, where the intersystem crossing process is obviously enhanced due to the heavy metal effect of the iridium atom. Figure 1e displays the transient decay curves of *fac*-Ir(tBufppy)$_3$ in PMMA film with a 2 wt.% doping ratio. *fac*-Ir(tBufppy)$_3$ exhibits a long lifetime of ≈1.71 µs as well as a high PLQY value of 76.5%, resulting in a large radiative rate (k_r) of 4.47×10^5 s^{-1} and a small non-radiative rate (k_{nr}) of 1×10^5 s^{-1}. These results illustrate the intense and highly efficient phosphorescent emission of *fac*-Ir(tBufppy)$_3$, implying the advantages of iridium complex as a photosensitizer or additive in photovoltaic applications. Table 1 summarizes the photophysical properties of *fac*-Ir(tBufppy)$_3$. The diagram scheme of the PL mechanism of

**ADVANCED
SCIENCE NEWS**

www.advancedsciencenews.com

**ADVANCED
FUNCTIONAL
MATERIALS**

www.afm-journal.de

Figure 3. a) Device structure diagram. b) J–V curves and c) EQE curves of the corresponding devices with different ratios of fac-Ir(tBufppy)$_3$. d) The PL spectra of PM6 neat films, control, and 10%fac-Ir(tBufppy)$_3$-based blend film. e) The PL spectra of fac-Ir(tBufppy)$_3$ and PM6 neat films, and PM6 with different ratios of fac-Ir(tBufppy)$_3$ blend films. f) The TRPL spectra of PM6 neat films, and PM6 with different ratios of fac-Ir(tBufppy)$_3$ blend films. g) The curves of J_{ph} versus V_{eff} in the optimized solar cells. h) The dependence of P_{light} on the J_{SC} of the optimized solar cells. i) The dependence of P_{light} on V_{OC} of the optimized solar cells.

fac-Ir(tBufppy)$_3$ is shown in Figure 2b based on all the above descriptions. Two distinct processes can be highlighted in OSCs through the introduction of fac-Ir(tBufppy)$_3$: one is that UV light can be effectively captured to generate a population of long-lived triplet excitons; the other is that the triplet emission energy can be reused by the host materials via Förster energy transfer mechanism.[35] Therefore, the photogenerated excitons in active layers should be significantly increased with the incorporation of fac-Ir(tBufppy)$_3$ phosphor, contributing to the higher J_{SC} and, thus, higher PCE of the corresponding devices.

2.3. Photovoltaic Properties

To estimate the photovoltaic performance of the corresponding devices, PM6:fac-Ir(tBufppy)$_3$:BTP-eC9 ternary OSCs were fabricated with fac-Ir(tBufppy)$_3$ as the third component. All OSCs were fabricated by maintaining the PM6:BTP-eC9 weight ratio as 1:1.2 with various contents of fac-Ir(tBufppy)$_3$ (0%, 5%, 10%, 20%, 30%, and 50% by weight of PM6) using a halogen-free solvent (O-XY). Although non-halogenated solvents generally have poorer solubility compared to halogenated solvents, as for a high-boiling-point solvent, O-XY can improve its solubility for BTP-eC9 under heating conditions, meeting the processing conditions. The device structure is ITO/PEDOT: PSS/Active layer/PFN-Br/Ag (**Figure 3a**), and the detail of the device preparation process is shown in ESI. The current density–voltage (J–V) curves of these OSCs are depicted in Figure 3b, and the corresponding device parameters are summarized in **Table 2**. The optimized host binary OSCs based on PM6:BTP-eC9 exhibited a PCE of 17.41% with an open-circuit voltage (V_{OC}) of 0.843, a J_{SC} of 26.99 mA cm^{-2}, and an FF of 76.52%, which is consistent with the related reported results.[36,37] We observed that with an increase in the fac-Ir(tBufppy)$_3$ content, the V_{OC} of the ternary device consistently decreased slightly, while J_{SC}, FF, and PCE initially increased and then decreased. The optimal performance

ADVANCED
SCIENCE NEWS
www.advancedsciencenews.com

ADVANCED
FUNCTIONAL
MATERIALS
www.afm-journal.de

Table 2. The photovoltaic parameters of the binary and ternary devices.

Third component ratio	V_{OC} [V]	J_{SC}[a] [mA cm^{-2}]	J_{SC}^{EQE} [mA cm^{-2}]	FF [%]	PCE$_{max}$[b] [%]
Control[c]	0.843	26.99	25.89	76.52	17.41 (17.18 ± 0.18)
5%*fac*-Ir(tBufppy)$_3$[c]	0.840	27.32	26.13	78.93	18.11 (17.89 ± 0.15)
10%*fac*-Ir(tBufppy)$_3$[c]	0.838	27.77	26.52	79.67	18.54 (18.35 ± 0.13)
20%*fac*-Ir(tBufppy)$_3$[c]	0.835	27.69	26.38	77.53	17.92 (17.76 ± 0.11)
30%*fac*-Ir(tBufppy)$_3$[c]	0.831	26.91	25.86	76.41	17.08 (16.81 ± 0.17)
50%*fac*-Ir(tBufppy)$_3$[c]	0.825	21.97	21.15	74.39	13.49 (13.20 ± 0.19)

[a] J_{SC} measured from devices; [b] PCE obtained from 15 devices, with 0.5% DIO additive; [c] PM6:*x*%Ir:A = 10:*x*%10:12 mg mL^{-1}, the concentration of PM6 is 10 mg mL^{-1}.

was achieved at a content of 10% (PCE = 18.54%), with V_{OC}, J_{SC}, and FF values of 0.838 V, 27.77 mA cm^{-2}, and 79.67%, respectively. The decrease in V_{OC} may be attributed to the higher HOMO energy level of *fac*-Ir(tBufppy)$_3$. The initial increase and subsequent decrease in other parameters may be explained by the fact that a small amount of *fac*-Ir(tBufppy)$_3$ can optimize the morphology of the active layer in the host binary. However, an excessive amount of *fac*-Ir(tBufppy)$_3$ may disrupt the stacking of molecules in the host binary system. These details will be elaborated in the subsequent morphology section. It is worth noting that FFs still achieve higher values of 74.39% in ternary devices (50%), which may result from the good compatibility of *fac*-Ir(tBufppy)$_3$ with the host component. The External Quantum Efficiency (EQE) spectra are illustrated in Figure 3c. The optimized ternary devices, featuring 10% *fac*-Ir(tBufppy)$_3$, demonstrated elevated EQE values in both the donor and acceptor absorption ranges compared to the control devices (0% *fac*-Ir(tBufppy)$_3$). Additionally, the J_{SC} values obtained from EQE spectral integration align closely with those acquired from the J–V measurement, with an error margin of less than 5% (Table 2). Furthermore, the absorption spectra of the blend films were measured to understand the impact of the iridium complex on photon harvesting within the active layer. As shown in Figure S4a,b (Supporting Information), adding a small amount of *fac*-Ir(tBufppy)$_3$ increases the absorption of the blend film, which explains why ternary devices with 10% and 30% *fac*-Ir(tBufppy)$_3$ maintain high J_{SC} and EQE. However, when the *fac*-Ir(tBufppy)$_3$ content is increased to 50%, the thickness of the blend film decreases, likely due to the reduced viscosity of the solution caused by the high concentration of small molecules. This leads to a significant drop in absorption intensity for the 50% *fac*-Ir(tBufppy)$_3$ ternary blend film, resulting in lower EQE and J_{SC} for the device.

2.4. Charge Separation, Transport and Recombination

To understand the enhancement of J_{SC} and FF in ternary OSCs, a PM6-based single component device and PM6:PM6:fac-Ir(tBufppy)3-based binary device were constructed, the J--V curves and corresponding parameters shown in Figure 3d and Table S2 (Supporting Information). The single-component device based on PM6 demonstrated a J_{SC} of 0.023 mA cm^{-2}, and an FF of 31.24%. However, in PM6:*fac*-Ir(tBufppy)$_3$-based binary device with varying ratios (ranging from 1:0.5, 1:1 to 1:1.5), the J_{SC} obviously improved from 0.029 to 0.043 mA cm^{-2}, with a corresponding rise in FF from 33.57% to 36.08%, while V_{OC} remained

almost constant. These significant improvements in J_{SC} and FF observed with the increasing content of *fac*-Ir(tBufppy)$_3$ strongly suggest the presence of energy transfer between PM6 and *fac*-Ir(tBufppy)$_3$.[38]

Furthermore, the steady-state PL and time-resolved PL (TRPL) were measured for the corresponding blend films, and the results are shown in Figure 3e,f and Figure S4a (Supporting Information). The PM6 neat film, control, and ternary blend films were excited with 580 nm of light, and an intense emission peak was observed in the PM6 neat film. The emission of the PM6 neat film is almost completely quenched in control and 10%Ir-based ternary blend films with high quenching efficiencies of 96.3% and 96.4%, respectively. The results show that both blend films exhibit efficient charge transfer from donor to acceptor.[39] To comprehend the enhancement observed in J_{SC} within the 10% Ir-based ternary system, PL spectra were acquired for *fac*-Ir(tBufppy)$_3$ and PM6 neat films, as well as PM6 films, blended with varying ratios of *fac*-Ir(tBufppy)$_3$ (Figure 3e). The PL range for *fac*-Ir(tBufppy)$_3$ and PM6 neat films spanned ≈500–600 and 650–800 nm, respectively. Upon the introduction of different ratios (5-50%) of *fac*-Ir(tBufppy)$_3$ into PM6 films, the PL signal originating from *fac*-Ir(tBufppy)$_3$ almost entirely vanished. Simultaneously, the PL intensity of PM6 markedly increased. To be more specific: At 0%, 5%, and 10% *fac*-Ir(tBufppy)$_3$, the PL intensity of blend films is obviously increase due to the effective energy transfer. At a larger ratio from 20% to 50%, the PL intensity displays a relatively slow growth but still larger that the control film, which should be attributed to the multiple interactions of energy transfer efficiency, film morphology, and varied composition. Moreover, TRPL measurements were employed to characterize both PM6 neat films and PM6 films blended with various proportions of *fac*-Ir(tBufppy)$_3$ (Figure 3f). The lifetime of the PM6 neat film was determined to be 0.216 ns, while the lifetimes of blend films for PM6, combined with different ratios (5–50%) of *fac*-Ir(tBufppy)$_3$, increased with the concentration of *fac*-Ir(tBufppy)$_3$. The respective lifetimes were 0.224, 0.229, 0.241, 0.265, and 0.304 ns. These phenomena suggest an efficient energy transfer from *fac*-Ir(tBufppy)$_3$ to PM6, elucidating the rationale behind the elevated J_{SC} observed in the 10% Ir-based ternary device.

The charge transport characteristics of the control and ternary blend films were examined using the space-charge limited current method, as illustrated in Figure S5 (Supporting Information) and tabulated in Table S5 (Supporting Information). The hole-only and electron-only device structures were ITO/PEDOT:PSS/Active Layer/MoO$_3$/Ag and ITO/ZnO/Active Layer/Ag,

**ADVANCED
SCIENCE NEWS**

www.advancedsciencenews.com

**ADVANCED
FUNCTIONAL
MATERIALS**

www.afm-journal.de

respectively. For the PM6:BTP-eC9 binary devices, the hole (μ_h) and electron (μ_e) mobilities were determined to be 1.71×10^{-4} and 2.91×10^{-4} cm^2 V^{-1} s^{-2}, respectively. Upon the incorporation of 10%, 30%, and 50% fac-Ir(tBufppy)$_3$, the μ_h values arrived to 1.97×10^{-4}, 1.61×10^{-4}, and 1.24×10^{-4} cm^2 V^{-1} s^{-2}, respectively, while the μ_e values were measured as 3.08×10^{-4}, 2.87×10^{-4}, and 2.49×10^{-4} cm^2 V^{-1} s^{-2}, respectively. Consequently, the μ_h/μ_e ratio for the control, 10%, 30%, and 50% fac-Ir(tBufppy)$_3$-based ternary devices was calculated to be 0.59, 0.64, 0.56, and 0.50, respectively. The marginally improved hole and electron mobilities upon adding 10% fac-Ir(tBufppy)$_3$ elucidates the rationale behind the enhanced FF in the optimized ternary device.

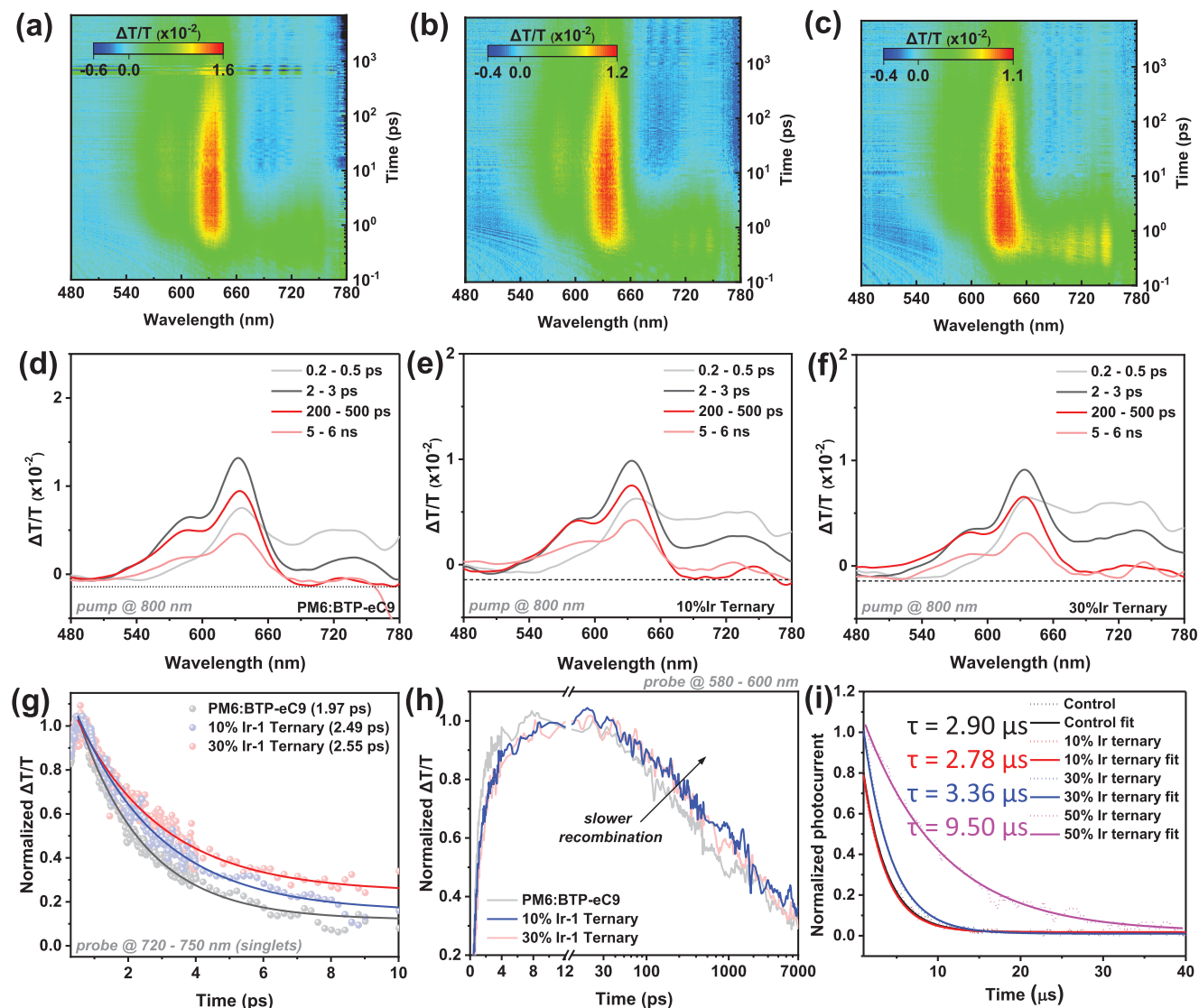The analysis of exciton dissociation and charge collection in OSCs commonly involves studying the photocurrent density (J_{ph}) versus effective voltage (V_{eff}) curves.[40] In this context, J_{ph} is defined as the difference between current densities under illumination (J_L) and in the dark (J_D). V_{eff} is determined as $V_0 - V_a$, where V_0 is the voltage when $J_{ph} = 0$, and V_a is the applied voltage. As depicted in Figure 3g, when $V_{eff} > 2$ V, J_{ph} reaches saturation, indicating efficient dissociation of nearly all excitons into electrons and holes. The exciton dissociation efficiency (η_d) is defined by the J_{ph}/J_{sat} values under short-circuit conditions. The η_d values for control, 10% fac-Ir(tBufppy)$_3$, 30% fac-Ir(tBufppy)$_3$, and 50% fac-Ir(tBufppy)$_3$-based devices are 0.963, 0.977, 0.961, and 0.948, respectively. This suggests a more efficient exciton dissociation in the 10% fac-Ir(tBufppy)$_3$-based ternary device. These findings demonstrate that incorporating appropriate amounts of fac-Ir(tBufppy)$_3$ as a third component in binary OSCs effectively enhances η_d, leading to simultaneous improvements in J_{SC} and FF. Furthermore, charge recombination is another significant factor influencing J_{SC} and FF, and it was investigated by establishing a relationship between J_{SC} or V_{OC} and light intensity (P_{light}). The light intensity (P_{light}) dependence of J_{SC} can be described by the relation $J_{SC} \propto (P_{light})^\alpha$, providing an insight into the charge recombination behavior in the devices. As depicted in Figure 3h, the fitted α values for the control, 10% fac-Ir(tBufppy)$_3$, 30% fac-Ir(tBufppy)$_3$, and 50% fac-Ir(tBufppy)$_3$-based devices are 0.97, 0.98, 0.96, and 0.95, respectively. This indicates the weakest bimolecular recombination in 10% fac-Ir(tBufppy)$_3$-based devices.[41] Additionally, the extent of trap-assisted recombination can be assessed through the relationship $V_{OC} \propto nKT/q\ln(P_{light})$, where n represents the ideality factor, K is the Boltzmann constant, T is the absolute temperature, and q is the elementary charge. The slope of this relationship indicates the predominant recombination type in OSCs. A slope of kT/q suggests that bimolecular recombination is the primary recombination mechanism, while a slope close to 2kT/q indicates significant trap-assisted recombination. As illustrated in Figure 3i, the slopes for control, 10% fac-Ir(tBufppy)$_3$, 30% fac-Ir(tBufppy)$_3$, and 50% fac-Ir(tBufppy)$_3$-based devices are 1.16, 1.12, 1.17, and 1.23 kT q^{-1}, respectively. This suggests the least trap-assisted recombination in 10% fac-Ir(tBufppy)$_3$-based ternary OSCs.[42,43]

To gain a deeper understanding of the underlying mechanisms responsible for the higher J_{SC} and FF in the 10% fac-Ir(tBufppy)$_3$-based ternary device, femtosecond transient absorption spectroscopy was employed to investigate the dynamics of photo-induced hole transfer and polaron recombination in these blend films. Specifically, an 800 nm pump laser beam selectively excited the acceptor material BTP-eC9, and the time-dependent spectral evolution was compared among the control, 10%, and 30% fac-Ir(tBufppy)$_3$-based blend films. In **Figure 4**, we present the 2D color plot and the corresponding spectral line cuts at various delay times. As the delay time progresses, a decay in the BTP-eC9 singlet excitons ground state bleach (GSB) intensity probed in the 680–770 nm range was observed, corresponding to excitons either dissociating to form free charges or decaying back to the ground state. Additionally, positive photo bleach peaks emerged in the 540–660 nm range (Figure 4d–f), aligning well with the absorption features of PM6 (Figure 1). Notably, pure BTP-eC9 exhibited no positive bleach at 480–620 nm (Figure S6, Supporting Information), indicating that singlet exciton dissociation through hole transfer occurred in the corresponding blend films with PM6. Furthermore, the observed decay process in the singlet excitons GSB is consistent with the rising positive polaron photo-bleach, suggesting efficient hole transfer at the interfaces between the donors and acceptors in the blend films. The decay lifetimes of singlet excitons in control, 10%Ir, and 30%Ir ternary blend films were determined to be 1.97, 2.49, and 2.55 ps, potentially attributed to the longer lifetime of the Ir-complex. However, this does not exclusively mean detrimental to charge generation, but instead more of describing the nanomorphology, mobilities, and interface energetics as other factors are imparting highly efficient charge generation despite a slower process.[44] In fact, the slower process can even assist and benefit charge generation.[45] Furthermore, investigation of polaron lifetimes (Figure 4h) revealed slightly slower sub-ns polaron recombination in the two ternary films, suggesting that the Ir-complex has the potential to suppress polaron recombination based on bimolecular recombination (i.e., known to be dominant at sub-ns regime), contributing to improved FF. Although the FF of 30%Ir-based devices is lower than that without Ir complex, it may be that 30%Ir complex has some detrimental effects in morphology, increasing the trap-assisted recombination (i.e., more observable beyond sub-ns regime) but also highly regulating the FF. Transient photocurrent (TPC) characterization was also performed to quantitatively analyze charge recombination and extraction in devices. As shown in Figure 4i, the photocurrent decay time of the control, 10%, 30%, and 50% fac-Ir(tBufppy)$_3$-based ternary devices were 2.90, 2.78, 3.36, and 9.50 μs, respectively, indicating that charge extraction in the 10% fac-Ir(tBufppy)$_3$-based ternary device is the most efficient.[46]

The grazing-incidence wide-angle X-ray scattering (GIWAXS) technique was employed to examine the molecular stacking and orientation of films. As depicted in **Figure 5a–f**, the (100) diffraction peak in the in-plane (IP) direction of the control blend film, as well as the 10%, 30%, and 50% fac-Ir(tBufppy)$_3$-based ternary blend films, is observed at 0.307 Å^{-1} ($d = 20.46$ Å, CCL = 74.37 Å), 0.308 Å^{-1} ($d = 20.39$ Å, CCL = 78.50 Å), 0.307 Å^{-1} ($d = 20.46$ Å, CCL = 78.50 Å), and 0.307 Å^{-1} ($d = 20.46$ Å, CCL = 74.37 Å), respectively. Furthermore, the (100) diffraction peaks in the out-of-plane (OOP) direction of the control blend film and the 10%, 30%, and 50% fac-Ir(tBufppy)$_3$-based ternary blend films are located at 0.308 Å^{-1} ($d = 20.39$ Å, CCL = 56.52 Å), 0.313 Å^{-1} ($d = 20.06$ Å, CCL = 64.96 Å), 0.329 Å^{-1} ($d = 19.08$ Å, CCL = 68.09 Å), and 0.330 Å^{-1} ($d = 19.03$ Å, CCL = 67.28 Å), respectively. The (010) diffraction peaks in the OOP direction of the control blend film and the 10%, 30%, and 50% fac-Ir(tBufppy)$_3$-based ternary blend films are consistently

**ADVANCED
SCIENCE NEWS**

www.advancedsciencenews.com

**ADVANCED
FUNCTIONAL
MATERIALS**

www.afm-journal.de

Figure 4. a–c) 2D color plot of fs-TA spectra of control, 10%*fac*-Ir(tBufppy)₃ and 30%*fac*-Ir(tBufppy)₃-based ternary blend at indicated delay times under 800 nm excitation with a fluence below 10 μJ cm⁻². d–f) The fs-TA spectra of control, 10%*fac*-Ir(tBufppy)₃ and 30%*fac*-Ir(tBufppy)₃-based ternary blend at indicated delay times. g) Lifetime of single exciton with the corresponding sum of exponential fittings. h) Hole polaron generation and recombination dynamics with the corresponding sum of exponential fittings. i) TPC diagram of control binary, 10%, 30%, and 50%*fac*-Ir(tBufppy)₃-based ternary devices.
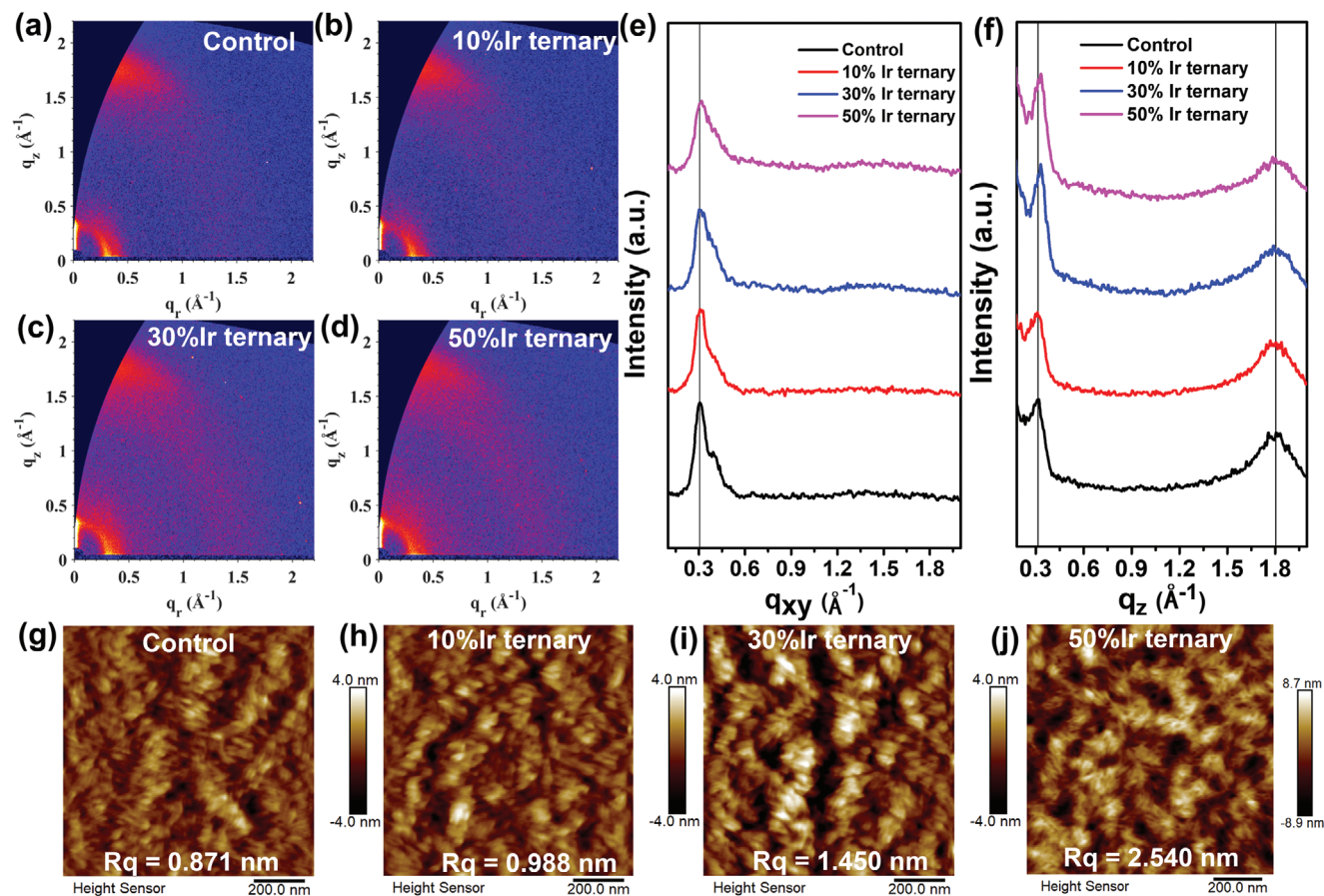
located at 1.80 Å⁻¹ (d = 3.48 Å), with corresponding similar CCLs of 22.79, 22.88, 22.43, and 22.33 Å, respectively. Based on the aforementioned results, it is evident that the introduction of 10% *fac*-Ir(tBufppy)₃ enhances lamella stacking of PM6 (the (100) peak located at ≈0.3 Å⁻¹) both in the IP and OOP directions, thereby benefiting charge transport,[47] which should be the main reason for the high FF of over 74% in all devices with 5–50% Ir complex.

To assess the impact of *fac*-Ir(tBufppy)₃ on morphology, tapping-mode atomic force spectroscopy (AFM) was employed to investigate the surface morphologies of the blend films, with AFM height images presented in Figure 5g–j. The blend films comprising the control, 10% *fac*-Ir(tBufppy)₃, 30% *fac*-Ir(tBufppy)₃, and 50% *fac*-Ir(tBufppy)₃-based ternary films exhibit a progressive increase in root-mean-square roughness

(0.871, 0.988, 1.450, and 2.540 nm, respectively). This trend suggests that the addition of *fac*-Ir(tBufppy)₃ facilitates the aggregation of donor and acceptor.[48] However, excessive addition leads to overlarge aggregates, inhibiting exciton dissociation. This phenomenon elucidates the rationale behind the superior performance observed in ternary devices based on 10%*fac*-Ir(tBufppy)₃, as it strikes a balance in promoting PM6 aggregation without hindering exciton dissociation.

The phase separation within the active layer is intrinsically influenced by the compatibility between donor and acceptor materials, a characteristic that can be elucidated through their respective surface energy parameters. Thus, contact angle measurements were employed to ascertain the surface energy values of each component. Figure S7 (Supporting Information) depicts the water contact angles for pristine films of PM6, BTP-eC9,

ADVANCED
SCIENCE NEWS

www.advancedsciencenews.com

ADVANCED
FUNCTIONAL
MATERIALS

www.afm-journal.de

Figure 5. 2D GIWAXS patterns of a) control, b) 10% *fac*-Ir(tBufppy)$_3$-based ternary film, c) 30% *fac*-Ir(tBufppy)$_3$-based ternary film, and d) 50% *fac*-Ir(tBufppy)$_3$-based ternary film. The 1D line cuts along e) in-plane and f) out-of-plane of the corresponding films. AFM images of g) control, h) 10% *fac*-Ir(tBufppy)$_3$-based ternary film, i) 30% *fac*-Ir(tBufppy)$_3$-based ternary film, and j) 50% *fac*-Ir(tBufppy)$_3$-based ternary film.

fac-Ir(tBufppy)$_3$, and blend film of PM6:10%*fac*-Ir(tBufppy)$_3$, measuring 103.568°, 93.336°, 93.377°, and 101.880°, respectively. Ethylene glycol (EG) contact angles were measured with the values of 74.386°, 64.121°, 65.241°, and 72.280°, respectively. According to Wu's model,[49] their corresponding surface energies were calculated as 25.206, 27.384, 26.663, and 25.776 mN m^{-1} (Table S3, Supporting Information). Moreover, the Flory–Huggins interaction parameter (χ) was applied to assess the compatibility between the components.[50] This parameter denoted as χ_{A-B}, which is determined by $\chi_{A-B} = K(\sqrt{\gamma_A} - \sqrt{\gamma_B})^2$, where γ_A and γ_B represents the surface energies of A and B, respectively. The resulting χ values, summarized in Table S3 (Supporting Information), were calculated as 0.0451, 0.0048, and 0.0243 K for $\chi_{PM6-BTP-eC9}$, $\chi_{fac-Ir(tBufppy)_3-BTP-eC9}$ and $\chi_{PM6:10\%fac-Ir(tBufppy)_3-BTP-eC9}$, respectively. The result shows that the surface energy of *fac*-Ir(tBufppy)$_3$ is between that of PM6 and BTP-eC9, which indicated *fac*-Ir(tBufppy)$_3$ shows good compatibility with PM6 and BTP-eC9. Furthermore, based on the χ values, the blend films of PM6:10% *fac*-Ir(tBufppy)$_3$ exhibit enhanced compatibility with BTP-eC9, suggesting that 10% *fac*-Ir(tBufppy)$_3$ optimizes the active layer morphology. This optimization is attributed to the superior FF observed in *fac*-Ir(tBufppy)$_3$-based ternary devices.

3. Conclusion

In summary, we synthesized a spatially stereo-structured metal complex, *fac*-Ir(tBufppy)$_3$, with strong phosphorescent emission, and took advantage of its long exciton lifetime for high-performance ternary PM6:*fac*-Ir(tBufppy)$_3$:BTP-eC9 device. We elucidated the functional mechanism of *fac*-Ir(tBufppy)$_3$ and systematically investigated its impact on the morphology of the active layer and the photovoltaic performance of the device. It is noteworthy that *fac*-Ir(tBufppy)$_3$ demonstrated excellent compatibility with the donor PM6 and acceptor BTP-eC9, maintaining the device efficiency above 90% of the optimal efficiency even with a 30% addition. In addition, transient absorption spectroscopy and transient PL measurements indicated the introduction of *fac*-Ir(tBufppy)$_3$ significantly prolonged the exciton lifetimes in the ternary device and effectively suppressed exciton recombination. In addition, we observed that the introduction of 10% *fac*-Ir(tBufppy)$_3$ was able to improve the lamellar aggregation of PM6 and improve the FF by optimizing the active layer morphology. Ultimately, by employing the non-halogenated solvent O-XY for processing, devices based on PM6:10% *fac*-Ir(tBufppy)$_3$:BTP-eC9 achieved an impressive PCE of 18.54%, surpassing the efficiency of binary PM6:BTP-eC9 devices (17.41%). This study

demonstrates a successful approach to synergistically prolonging exciton lifetime and modifying the morphology of the active layer to improve device performance. The development of a new iridium indophosphor that exhibits favorable energy level alignment and compatibility with host materials is a pivotal focus in the future molecular design for highly efficient green solvent-processed OSCs.

Conflict of Interest

The authors declare no conflict of interest.

Author Contributions

H.X. was involved in all the work and contributed to the manuscript writing. M.Z. completed the synthesis and characterizations of the Ir complex, as well as revised the manuscript. H.W., Y.S., and Z.L. provided help with materials synthesis, TRPL/PLQY test, and DFT calculations, respectively. R.M., T.A.D.P., M.L., and J.W. provided the TAS measurements. H.L. and X.L. provided the GIWAXS measurements. G.L. and W.-Y.W. supervised the project and contributed to the revision of the manuscript.

Data Availability Statement

The data that support the findings of this study are available from the corresponding author upon reasonable request.

[1] G. Li, V. Shrotriya, J. Huang, Y. Yao, T. Moriarty, K. Emery, Y. Yang, *Nat. Mater.* **2005**, *4*, 864.

[2] G. Li, R. Zhu, Y. Yang, *Nat. Photonics* **2012**, *6*, 153.

[3] L. Dou, Y. Liu, Z. Hong, G. Li, Y. Yang, *Chem. Rev.* **2015**, *115*, 12633.

[4] J. Hou, O. Inganäs, R. H. Friend, F. Gao, *Nat. Mater.* **2018**, *17*, 119.

[5] Y. Lin, J. Wang, Z.-G. Zhang, H. Bai, Y. Li, D. Zhu, X. Zhan, *Adv. Mater.* **2015**, *27*, 1170.

[6] J. Yuan, Y. Zhang, L. Zhou, G. Zhang, H.-L. Yip, T.-K. Lau, X. Lu, C. Zhu, H. Peng, P. A. Johnson, M. Leclerc, Y. Cao, J. Ulanski, Y. Li, Y. Zou, *Joule* **2019**, *3*, 1140.

[7] H. Yin, C. Yan, H. Hu, J. K. W. Ho, X. Zhan, G. Li, S. K. So, *Mater. Sci. Eng. R* **2020**, *140*, 100542.

[8] C. Wang, Q. Chen, C. Zhang, B. Han, X. Liu, S. Liang, B. Wang, C. Xiao, B. Gao, Z. Tang, G. Lu, L. Ding, W. Li, *CCS Chem.* **2024**, 1, https://doi.org/10.31635/ccschem.024.202404023.

[9] J. Fu, Q. Yang, P. Huang, S. Chung, K. Cho, Z. Kan, H. Liu, X. Lu, Y. Lang, H. Lai, F. He, P. W. K. Fong, S. Lu, Y. Yang, Z. Xiao, G. Li, *Nat. Commun.* **2024**, *15*, 1830.

[10] L. Guo, Q. Li, J. Ren, Y. Xu, J. Zhang, K. Zhang, Y. Cai, S. Liu, F. Huang, *Energy Environ. Sci.* **2022**, *15*, 5137.

[11] F. Zhao, C. Wang, X. Zhan, *Adv. Energy Mater.* **2018**, *8*, 1703147.

[12] L. Zhang, D. Deng, K. Lu, Z. Wei, *Adv. Mater.* **2023**, *36*, 2302915.

[13] M. Jiang, H.-r. Bai, H.-f. Zhi, J.-k. Sun, J.-l. Wang, F. Zhang, Q. An, *ACS Energy Lett.* **2021**, *6*, 2898.

[14] Z. Wang, Z. Peng, Z. Xiao, D. Seyitliyev, K. Gundogdu, L. Ding, H. Ade, *Adv. Mater.* **2020**, *32*, 2005386.

[15] H.-Y. Wei, J.-H. Huang, C.-Y. Hsu, F.-C. Chang, K.-C. Ho, C.-W. Chu, *Energy Environ. Sci.* **2013**, *6*, 1192.

[16] X. Liu, Y. Yan, A. Honarfar, Y. Yao, K. Zheng, Z. Liang, *Adv. Sci.* **2019**, *6*, 1802103.

[17] Y. Cai, Q. Li, G. Lu, H. S. Ryu, Y. Li, H. Jin, Z. Chen, Z. Tang, G. Lu, X. Hao, H. Y. Woo, C. Zhang, Y. Sun, *Nat. Commun.* **2022**, *13*, 2369.

[18] Q. Guo, Y. Liu, M. Liu, H. Zhang, X. Qian, J. Yang, J. Wang, W. Xue, Q. Zhao, X. Xu, W. Ma, Z. Tang, Y. Li, Z. Bo, *Adv. Mater.* **2020**, *32*, 2003164.

[19] L. Zhang, M. Zhang, Y. Ni, W. Xu, H. Zhou, S. Ke, H. Tian, S. Y. Jeong, H. Y. Woo, W. Y. Wong, X. Ma, F. Zhang, *ACS Materials Lett.* **2024**, *6*, 2964.

[20] M. Zhang, M. N. A. S. Ivan, Y. Sun, Z. Li, S. Saha, S. Ahmed, H. Liu, Y. Wang, Y. H. Tsang, W. Y. Wong, *J. Mater. Chem. A* **2024**, *12*, 9055.

[21] H. Zhou, Y. Sun, M. Zhang, Y. Ni, F. Zhang, S. Y. Jeong, T. Huang, X. Li, H. Y. Woo, J. Zhang, W. Y. Wong, X. Ma, F. Zhang, *Sci. Bulletin* **2024**, https://doi.org/10.1016/j.scib.2024.07.027.

[22] T. Yang, B. Wang, Y. He, A. Zhou, Z. Yao, G. Xing, Y. Tao, *Inorg. Chem.* **2023**, *62*, 5920.

[23] M. Zhang, X. Ma, H. Zhang, L. Zhu, L. Xu, F. Zhang, C.-S. Tsang, L. Y. S. Lee, H. Y. Woo, Z. He, W.-Y. Wong, *Chem. Eng. J.* **2022**, *430*, 132832.

[24] K. Zhou, K. Xian, L. Ye, *InfoMat* **2022**, *4*, e12270.

[25] S. Liang, W. Li, L. Ding, *J. Semicond.* **2023**, *44*, 030201.

[26] E. Feng, C. Zhang, J. Chang, H. Li, L. Ding, J. Yang, *J. Semicond.* **2024**, *45*, 050201.

[27] W. Feng, S. Wu, H. Chen, L. Meng, F. Huang, H. Liang, J. Zhang, Z. Wei, X. Wan, C. Li, Z. Yao, Y. Chen, *Adv. Energy Mater.* **2022**, *12*, 2104060.

[28] M. Zhang, W. Gao, F. Zhang, Y. Mi, W. Wang, Q. An, J. Wang, X. Ma, J. Miao, Z. Hu, X. Liu, J. Zhang, C. Yang, *Energy Environ. Sci.* **2018**, *11*, 841.

[29] H. Xia, Y. Zhang, W. Deng, K. Liu, X. Xia, C. J. Su, U. S. Jeng, M. Zhang, J. Huang, J. Huang, C. Yan, W. Y. Wong, X. Lu, W. Zhu, G. Li, *Adv. Mater.* **2022**, *34*, 2107659.

[30] M. Zhang, F. Zhang, Q. An, Q. Sun, W. Wang, J. Zhang, W. Tang, *Nano Energy* **2016**, *22*, 241.

[31] X. Xu, K. Feng, Z. Bi, W. Ma, G. Zhang, Q. Peng, *Adv. Mater.* **2019**, *31*, 1901872.

[32] T. Wang, R. Sun, M. Shi, F. Pan, Z. Hu, F. Huang, Y. Li, J. Min, *Adv. Energy Mater.* **2020**, *10*, 2000590.

[33] Z.-C. Wen, H. Yin, X.-T. Hao, *Surf. Interfaces* **2021**, *23*, 100921.

[34] Y. Cui, H. Yao, J. Zhang, K. Xian, T. Zhang, L. Hong, Y. Wang, Y. Xu, K. Ma, C. An, C. He, Z. Wei, F. Gao, J. Hou, *Adv. Mater.* **2020**, *32*, 1908205.

[35] V. Gupta, V. Bharti, M. Kumar, S. Chand, A. J. Heeger, *Adv. Mater.* **2015**, *27*, 4398.

[36] J. W. Lee, C. Lim, S. W. Lee, Y. Jeon, S. Lee, T. S. Kim, J. Y. Lee, B. J. Kim, *Adv. Energy Mater.* **2022**, *12*, 2202224.

[37] M. Li, K. Zhang, J. Qiao, Q. Wang, L. Wang, M. Sun, L. Ying, N. Li, P. Lu, H. Yin, X. Du, X. Hao, *Adv. Funct. Mater.* **2023**, *33*, 2214361.

[38] M. Zhang, J. Wang, X. Ma, J. Gao, C. Xu, Z. Hu, L. Niu, F. Zhang, *APL Mater.* **2020**, *8*, 090703.

[39] Y. Chen, R. Ma, T. Liu, Y. Xiao, H. K. Kim, J. Zhang, C. Ma, H. Sun, F. Bai, X. Guo, K. S. Wong, X. Lu, H. Yan, *Adv. Energy Mater.* **2021**, *11*, 2003777.

[40] P. W. M. Blom, V. D. Mihailetchi, L. J. A. Koster, D. E. Markov, *Adv. Mater.* **2007**, *19*, 1551.

[41] L. Nian, K. Gao, Y. Jiang, Q. Rong, X. Hu, D. Yuan, F. Liu, X. Peng, T. P. Russell, G. Zhou, *Adv. Mater.* **2017**, *29*, 1700616.

[42] L. J. A. Koster, V. D. Mihailetchi, R. Ramaker, P. W. M. Blom, *Appl. Phys. Lett.* **2005**, *86*, 123509.

[43] H. Xia, Y. Zhang, K. Liu, W. Deng, M. Zhu, H. Tan, P. W. K. Fong, H. Liu, X. Xia, M. Zhang, T. A. Dela Peña, R. Ma, M. Li, J. Wu, Y. Lang, J. Fu, W.-Y. Wong, X. Lu, X. Zhu, G. Li, *Energy Environ. Sci.* **2023**, *16*, 6078.

[44] T. A. Dela Peña, R. Ma, Z. Xing, Q. Wei, J. I. Khan, R. M. Young, Y. Hai, S. A. Garcia, X. Zou, Z. Jin, F. L. Ng, K. L. Yeung, D. F. Swearer, M. R. Wasielewski, J. Wang, H. Cha, H. Yan, K. S. Wong, G. Li, M. Li, J. Wu, *Energy Environ. Sci.* **2023**, *16*, 3416.

[45] S.-i. Natsuda, T. Saito, R. Shirouchi, Y. Sakamoto, T. Takeyama, Y. Tamai, H. Ohkita, *Energy Environ. Sci.* **2022**, *15*, 1545.

[46] S. Luo, C. Li, J. Zhang, X. Zou, H. Zhao, K. Ding, H. Huang, J. Song, J. Yi, H. Yu, K. S. Wong, G. Zhang, H. Ade, W. Ma, H. Hu, Y. Sun, H. Yan, *Nat. Commun.* **2023**, *14*, 6964.

[47] J. Rivnay, S. C. B. Mannsfeld, C. E. Miller, A. Salleo, M. F. Toney, *Chem. Rev.* **2012**, *112*, 5488.

[48] J. Cai, X. Zhang, C. Guo, Y. Zhuang, L. Wang, D. Li, D. Liu, T. Wang, *Adv. Funct. Mater.* **2021**, *31*, 2102189.

[49] Q. An, J. Wang, X. Ma, J. Gao, Z. Hu, B. Liu, H. Sun, X. Guo, X. Zhang, F. Zhang, *Energy Environ. Sci.* **2020**, *13*, 5039.

[50] X. Liu, C. Zhang, C. Duan, M. Li, Z. Hu, J. Wang, F. Liu, N. Li, C. J. Brabec, R. A. J. Janssen, G. C. Bazan, F. Huang, Y. Cao, *J. Am. Chem. Soc.* **2018**, *140*, 8934.

2411058 (11 of 11)